BRAIN COMMUNICATIONS

Persistent sodium currents in *SCN1A* developmental and degenerative epileptic dyskinetic encephalopathy

Kathleen M. Gorman,[1,2,*] Colin H. Peters,[3,4,*] Bryan Lynch,[1] Laura Jones,[3] Dani S. Bassett,[5,6] Mary D. King,[1,2] Peter C. Ruben[3] and Richard E. Rosch[7,8,9]

* These authors contributed equally to this work.

Pathogenic variants in the voltage-gated sodium channel gene (*SCN1A*) are amongst the most common genetic causes of childhood epilepsies. There is considerable heterogeneity in both the types of causative variants and associated phenotypes; a recent expansion of the phenotypic spectrum of *SCN1A* associated epilepsies now includes an early onset severe developmental and epileptic encephalopathy with regression and a hyperkinetic movement disorder. Herein, we report a female with a developmental and degenerative epileptic-dyskinetic encephalopathy, distinct and more severe than classic Dravet syndrome. Clinical diagnostics indicated a paternally inherited c.5053G>T; p. A1685S variant of uncertain significance in *SCN1A*. Whole-exome sequencing detected a second *de novo* mosaic (18%) c.2345G>A; p. T782I likely pathogenic variant in *SCN1A* (maternal allele). Biophysical characterization of both mutant channels in a heterologous expression system identified gain-of-function effects in both, with a milder shift in fast inactivation of the p. A1685S channels; and a more severe persistent sodium current in the p. T782I. Using computational models, we show that large persistent sodium currents induce hyper-excitability in individual cortical neurons, thus relating the severe phenotype to the empirically quantified sodium channel dysfunction. These findings further broaden the phenotypic spectrum of *SCN1A* associated epilepsies and highlight the importance of testing for mosaicism in epileptic encephalopathies. Detailed biophysical evaluation and computational modelling further highlight the role of gain-of-function variants in the pathophysiology of the most severe phenotypes associated with *SCN1A*.

1 Department of Neurology and Clinical Neurophysiology, Children's Health Ireland at Temple Street, Dublin, Ireland
2 School of Medicine and Medical Science, University College Dublin, Dublin, Ireland
3 Department of Biomedical Physiology and Kinesiology, Simon Fraser University, Burnaby, Canada
4 Department of Physiology and Biophysics, University of Colorado, Denver, CO, USA
5 Departments of Bioengineering, Electrical & Systems Engineering, Physics & Astronomy, Neurology, and Psychiatry, University of Pennsylvania, Philadelphia, PA, USA
6 Santa Fe Institute, Santa Fe, NM, USA
7 Department of Paediatric Neurology, Great Ormond Street Hospital for Children NHS Foundation Trust, London, UK
8 Department of Bioengineering, University of Pennsylvania, Philadelphia, PA, USA
9 MRC Centre for Neurodevelopmental Disorders, Institute of Psychiatry, Psychology and Neuroscience, King's College London, London, UK

Correspondence to: Richard E. Rosch, MRCPCH, PhD, MRC
Centre for Neurodevelopmental Disorders, Institute of Psychiatry, Psychology and Neuroscience
New Hunt's House, Great Maze Pond, London SE1 1UL, UK
E-mail: richard.rosch@doctors.org.uk

Keywords: epileptic encephalopathy; SCN1A; non-inactivating current; Hodgkin–Huxley model; sodium-channel gating

Received June 2, 2021. Revised June 15, 2021. Accepted June 21, 2021. Advance Access publication October 7, 2021

Abbreviations: DEE = developmental and epileptic encephalopathy; DS = Dravet syndrome; GEFS+ = generalized epilepsy with febrile seizures plus; GOF = gain-of-function; LOF =loss-of-function; WT = wildtype

Graphical Abstract

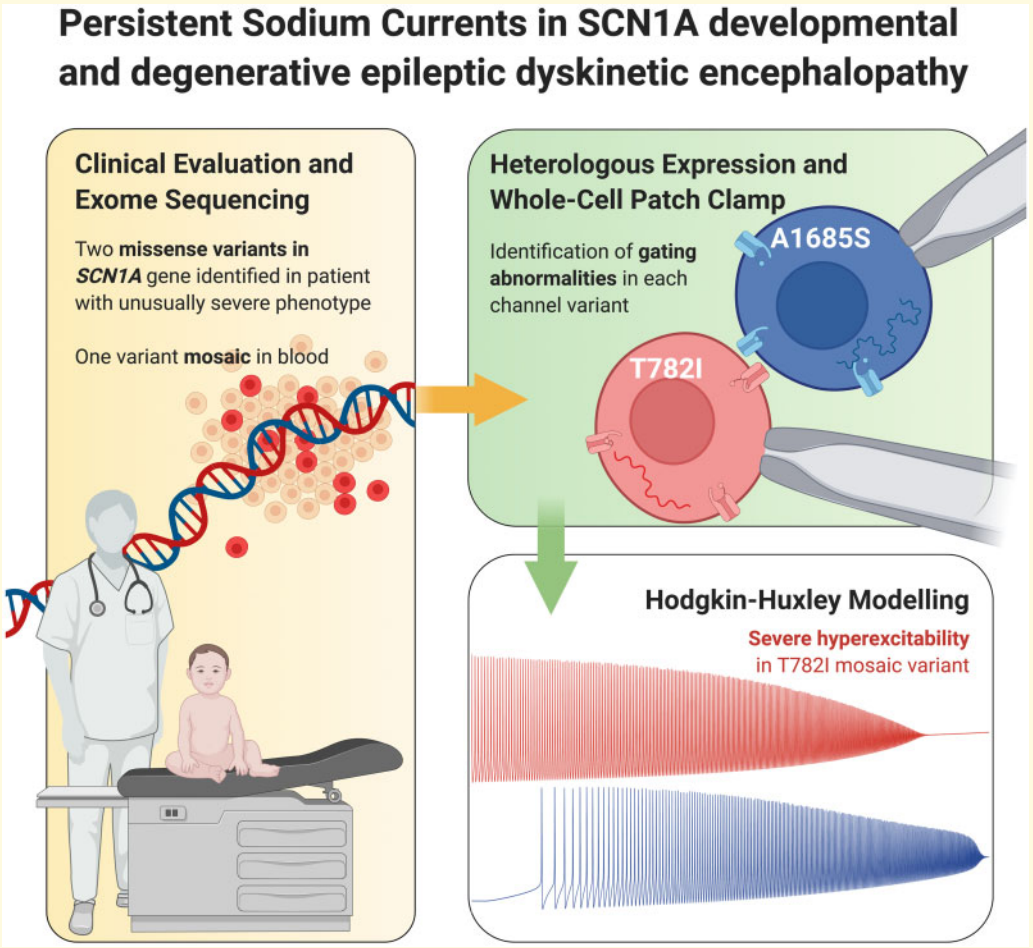

Note:Created with BioRender.com

Introduction

Developmental and epileptic encephalopathies (DEE) are a severe and rare group of epileptic encephalopathies that are characterized by early-onset epilepsy, which is typically refractory to anti-seizure medications, and is associated with developmental delay and/or regression, intellectual disability and multiple comorbidities (behavioural issues, enteral feeding, etc.).[1–3] This condition can refer to previously developmentally normal children, in which the epileptiform activity interferes with development, thereby resulting in cognitive slowing or regression.[3] There is a subset of children with DEE and a hyperkinetic movement disorder (choreoathetosis, dyskinesia, dystonia and non-epileptic myoclonus), who follow a neurodegenerative course with early mortality, independent of seizure control.[4–6] Developmental and degenerative epileptic-dyskinetic encephalopathy is the emerging term to describe this severe phenotype of DEE.[5]

The first identified genetic cause of DEE is the sodium channel neuronal type 1 alpha gene (*SCN1A*, Chr2:165,984,640–166,149,160 [GRCh38]), which encodes the neuronal voltage-gated sodium channel $Na_v1.1$. In mouse models, *SCN1A* is predominantly expressed in both parvalbumin and somatostatin positive inhibitory interneurons, and selective deletion in GABAergic neurons is sufficient to cause an epileptic phenotype.[7,8] *SCN1A* now accounts for a significant proportion of both DEE and a wider spectrum of genetic epilepsies.[9,10] Heterozygous variants in *SCN1A* are associated with a wide range of epilepsy phenotypes from severe DEE's such as Dravet syndrome (DS) (MIM:607208) or epilepsy of infancy with migrating focal seizures (MIM:607208) to self-limited and pharmaco-responsive epilepsies

including generalized epilepsy with febrile seizures plus (GEFS+) (MIM:604403).[10–13] With increased clinical testing afforded by next-generation sequencing, rarer but distinct *SCN1A* phenotypes are emerging, such as an early-onset *SCN1A* DEE with regression and a hyperkinetic movement disorder, distinct from DS.[14] Furthermore, technological advances now allow the identification of the clinical importance of mosaicism in *SCN1A*.[15–17]

Even though greater than 1200 variants are reported in *SCN1A* in DS alone, consistent predictions of phenotype from genotype remain elusive.[18] Loss-of-function (LOF), gain-of-function (GOF), and mixed LOF and GOF effects are all reported in individual cases.[13,19–23] *In silico* prediction tools are currently unable to predict the impact of channel function and the subsequent epilepsy phenotype and/or cognitive outcomes (DS versus GEFS+).[21] Despite the lack of one-to-one genotype–phenotype mapping, some general trends have been observed: LOF (missense and protein-truncating) variants typically cause classical DS, while only partial LOF results in GEFS+, a milder epilepsy phenotype.[21] GOF missense variants are only recently recognized as causative of a distinctive early-onset severe *SCN1A*- DEE, differentiated from DS by age of onset, clinical phenotype and cognitive outcome.[14] Although recent machine learning approaches suggest that further improvements *in silico* predictions are possible,[24] any such predictions will need to be validated against actual measurements of channel behaviour. Therefore, *in vitro* electrophysiological analysis of missense variants is still required in order to understand how variant-specific dysfunction in the $Na_v1.1$ channel can help to accurately predict clinical phenotypes, including response to medications and seizure burden.[24]

Here, we report clinical features, *in vitro* channel biophysical measurements, and *in silico* modelling results for a patient with a novel *SCN1A* variant and an unusually severe phenotype: DEE with additional profound developmental regression and hyperkinetic movement disorder, mimicking a neurodegenerative disease, with biallelic missense variants in *SCN1A* (inherited c.5053G>T; p. A1685S (paternal allele) variant of uncertain significance/*de novo* mosaic (18%) c.2345G>A; p. T782I likely pathogenic variant). When expressed in CHOK1 cells, both A1685S and T782I $Na_v1.1$ channels express functional sodium currents with distinct gating abnormalities compared to wildtype (WT) currents. At physiological temperatures the T782I mutant, both when expressed alone and when co-expressed with A1685S, produces a large non-inactivating sodium current. Implementing these gating behaviours in a Hodgkin–Huxley model of the neuronal membrane demonstrates a GOF effect in the T782I allele, which renders neurons more excitable at much lower input currents. These results highlight the role of *SCN1A* GOF and non-inactivating current in developmental and degenerative epileptic-dyskinetic encephalopathy, distinct from DS.

Materials and methods

Clinical evaluation

A female infant was born after an uneventful pregnancy and delivery to unrelated Caucasian parents with no family history of epilepsy or febrile seizures. Early developmental milestones were achieved until the onset of epilepsy. She presented aged 13 months with recurrent prolonged clonic and hemi-clonic seizures (1 febrile and 7 afebrile, 10–40 min in duration). The initial EEG showed a slow background and multi-focal epileptiform discharges, with a maximum in temporal regions (Fig. 1). From 15 months of age, daily frequent epileptic myoclonus (legs, arm or mouth) emerged and were associated with cognitive and motor regression (ceased vocalizing, progressive ataxia with loss of ambulation). Repeat EEG mirrored clinical progression with evolution to an epileptic encephalopathy with a slow background (1–3 Hz) and frequent multifocal bisynchronous epileptiform spike-wave (2 Hz) discharges which became continuous in sleep (Fig. 2). By age 20 months, there was almost continuous myoclonus with tonic, atypical absences, focal and frequent bilateral tonic-clonic (BTC) seizures with progressive pathology on the EEG (Fig. 3). There was no benefit from multiple combinations of anti-epileptic medications including: Carbamazepine, Clobazam, Clonazepam, Ethosuximide, Lacosamide, Levetiracetam, Nitrazepam, Rufinamide, Sodium Valproate, Stiripentol, Topiramate and steroids. There was a reduction in myoclonus after the insertion of a vagal nerve stimulator, though the reduction was not sustained. Frequent daily seizures occurred until her death. A hyperkinetic movement disorder was noted from 18 months of age, characterized predominantly by non-epileptic myoclonus, and additionally with a combination of dyskinesia, choreoathetosis and peri-oral dyskinesia, exacerbated by illness (Supplementary Video). This pattern was captured on EEG on multiple occasions without electrographic correlation. She was non-ambulant with little spontaneous movement (GMFCS Level 5), non-verbal, enterally fed, with neuropathic pain and dysautonomia. From 18 months of age, there was recurrent aspiration pneumonia, progressive respiratory muscle weakness and ventilatory failure requiring non-invasive ventilation. She died aged 6.5 years due to pneumonia.

Investigations

Chromosomal analysis, array comparative genomic hybridization and single-gene testing were negative (*EPM1, MECP2*, *PCDH19* and *POLG1*). A missense variant in *SCN1A*, chr2:166848732, c.5053C>A, p. Ala1685Ser was identified (Scotland Direct PCR amplification and bi-directional DNA sequencing of *SCN1A*). This variant was also present in her phenotypically normal father and was, therefore, assumed not to be disease-causing.

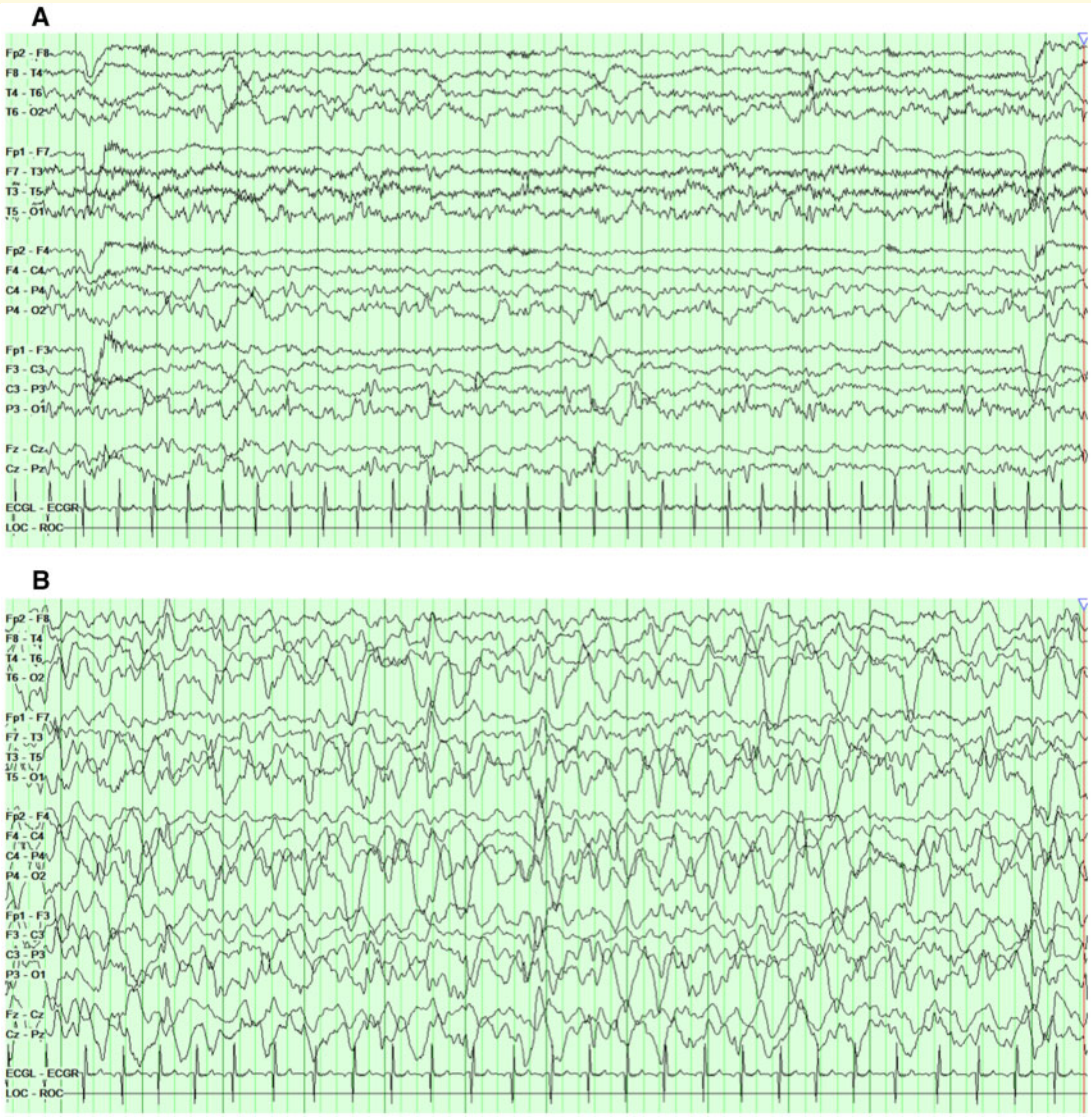

Figure 1 EEG aged 15 months. (**A**) (Awake) and (**B**) (sleep): EEG (HF filter, 70 Hz, sensitivity, 20 mV/mm; timebase, 30 mm/s) showing a slow awake background (mainly theta activity) and infrequent sharp waves. In sleep, epileptiform sharp waves were activated in bilateral temporal regions.

An extended metabolic profile (serum amino acids, lactate, ammonia, creatine kinase, transferrin isoforms, acylcarnitine, carnitine, very long chain fatty acids, lysosomal enzymes, urinary organic acids, CSF lactate and amino acids) and skin biopsy for neuronal ceroid lipofuscinosis were negative. Magnetic resonance imaging of the brain including MRS aged 13 months and 33 months were normal. Neuroimaging performed at 4 years of age showed non-specific cortical atrophy (Supplementary Fig. S1).

Whole-exome sequencing

Research whole-exome sequencing was performed as detailed in a previous study,[25] which also included the patient reported here (patient ID 42). Briefly, patients underwent whole-exome sequencing at Atlas Biolabs (http://www.atlas-biolabs.de), with standard bioinformatics analysis including sequence alignment, data cleaning and variant identification, targeting 137 known epilepsy-associated genes.[25] A trio (parent and proband) whole-exome sequencing was subsequently performed. The criteria for calling of heterozygous variants was updated from 25% to 15%, after the initial analysis to aid the identification of mosaic variants.

Fibroblasts

Confirmation was performed by CeGaT GmBH, Tübingen, Germany. The relevant region of the region

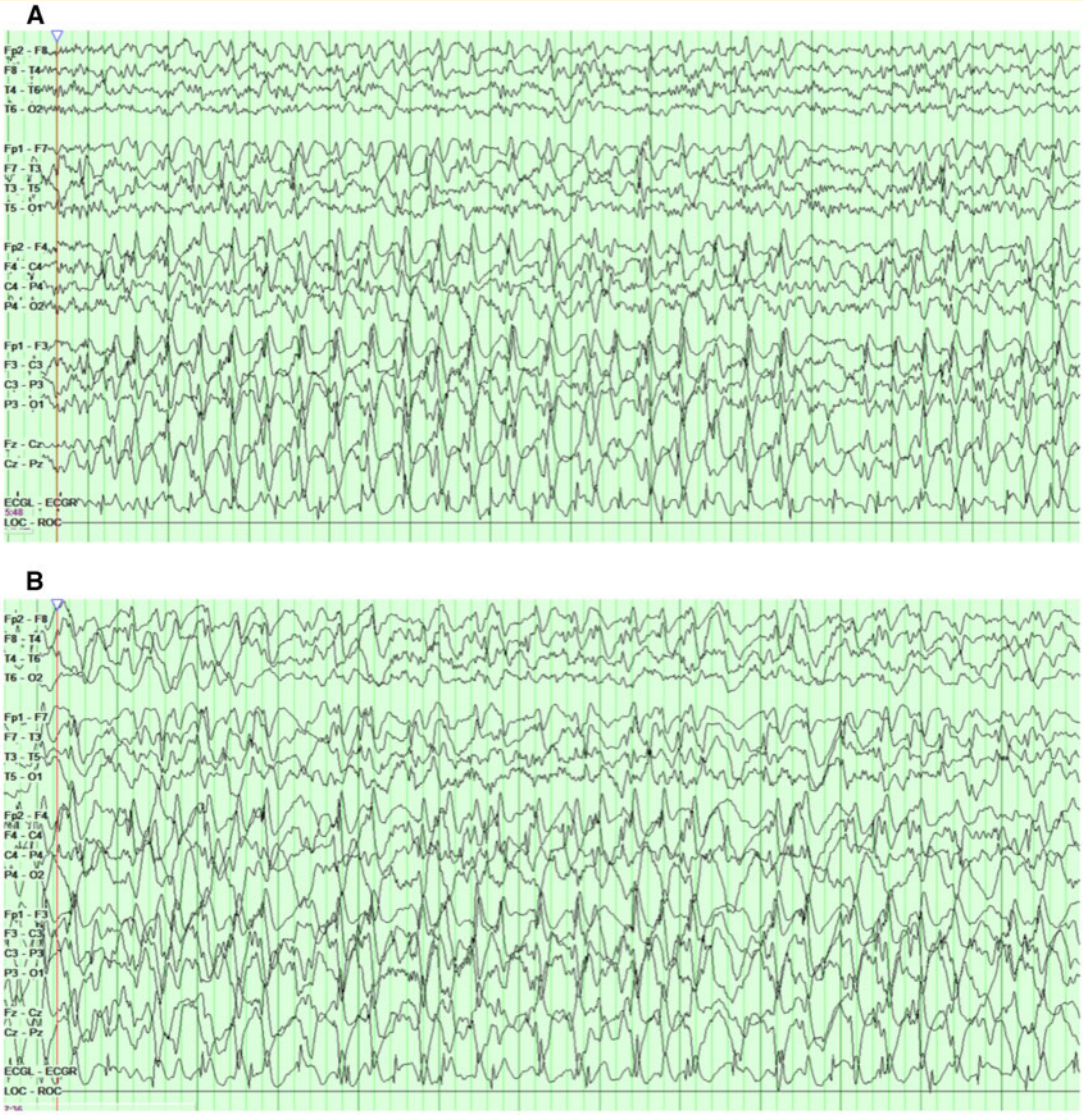

Figure 2 EEG aged 23 months. (**A**) (Awake) and (**B**) (sleep): EEG (HF filter, 70 Hz, sensitivity, 30 mV/mm; timebase, 30 mm/s) showing an epileptic encephalopathy with slow-wave and spike 2.5 Hz epileptiform discharges. Activation of continuous generalized epileptiform discharges in sleep.

was amplified by PCR and subsequently analysed by primer extension method (SNaPshot®, ThermoFisher) and capillary electrophoresis.

Bacterial transformations and mutagenesis

The WT PCDM8-SCN1A plasmid used in this study was described previously.[22] A Quikchange lightning site-directed mutagenesis kit was used to make both the c.2345 C > T (p. Thr782Ile) and c.5053 G > T (p. Ala1685Ser) mutants in the PCDM8-SCN1A plasmid. All DNA was grown in TOP10-P3 *E. coli*. at 30°C and the entire length of the insert was sequenced to check for spontaneous mutations or rearrangements.

We grew CHOK1 cells in Ham's F12 media supplemented with 10% FBS at 37°C and 5% CO2. Forty-eight hours prior to patch-clamp experiments 1 µg of PCDM8-SCN1A, 0.5 µg of SCN1B and 1 µg of eGFP DNA were transfected into CHOK1 cells on a 60 mm dish using 20 µl of Polyfect transfection reagent (Qiagen) according to the manufacturer's instructions. For experiments on co-transfected T782I/A1685S channels, 1 µg of DNA for each mutant was used. Twenty-four hours prior to patch-clamp experiments, cells were plated on sterile glass coverslips that fit in the recording chamber.

Electrophysiology

Whole-cell patch-clamp experiments were performed at 32°C and 37°C using borosilicate glass pipettes pulled

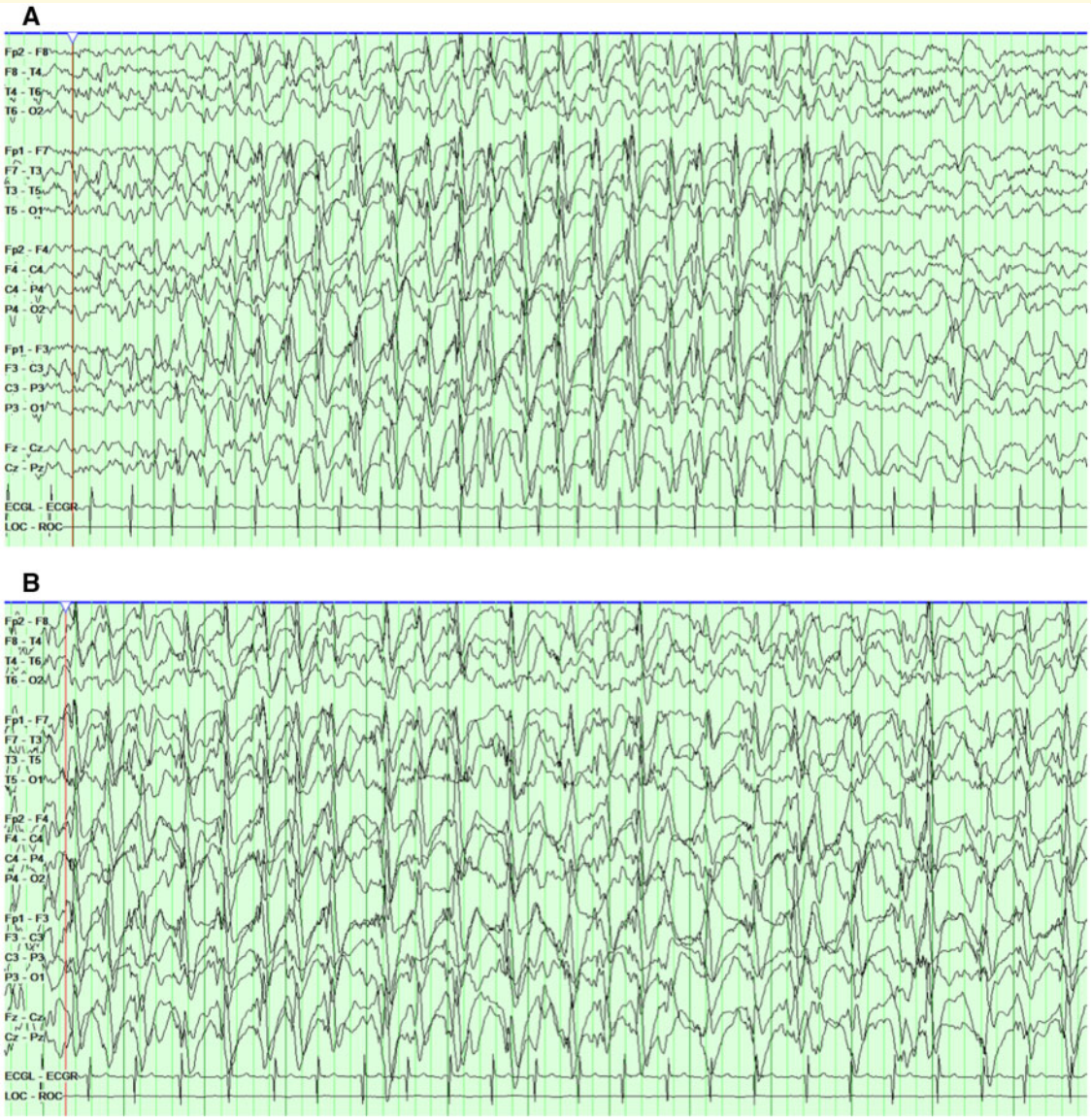

Figure 3 EEG aged 3 years. (**A**) (Atypical absence during awake state) and (**B**) (sleep): EEG (HF filter, 70 Hz, sensitivity, 30 mV/mm; timebase, 30 mm/s). Clinical event characterized by staring and cessation of hyperkinetic movements for 8 s with an EEG correlation of high-amplitude generalized regular 2Hz discharges. The epileptiform discharges become continuous in sleep.

with a P-1000 puller (Sutter Instruments, CA, USA). Pipettes were dipped in dental wax and polished to a resistance of 1.0–1.5 MΩ. Extracellular solutions contained (in mM): 140 NaCl, 4 KCl, 2 $CaCl_2$, 1 $MgCl_2$ and 10 HEPES. Intracellular solutions contained (in mM): 130 CsF, 10 NaCl, 10 HEPES and 10 EGTA. Extracellular and intracellular solutions were titrated to pH 7.4 with CsOH.

We performed all experiments using an EPC9 patch-clamp amplifier. Data were digitized using an ITC-16 interface (HEKA Elektronik, Lambrecht, Germany). For data collection and analysis, we used Patchmaster/Fitmaster (HEKA Elektronik) and Igor Pro (Wavemetrics, OR, USA) running on an iMac (Apple Inc., CA, USA). Temperature was maintained using a TC-10 temperature controller (Dagan Corporation, MN, USA). We applied a low-pass filter to the data at 10 kHz and used a P/4 leak subtraction procedure for all recordings. The holding potential between protocols was −90 mV.

To measure channel activation, cells were depolarized for 20 ms in 5 mV increments to membrane potentials between −100 mV and +60 mV from a pre-pulse potential of −130 mV. The equilibrium potential for any given cell was calculated by fitting a straight line to the peak currents recorded at more depolarized potentials and determining the zero current voltage. To calculate conductance, peak current at a given membrane potential was divided by the membrane potential minus the

measured equilibrium potential. Normalized conductance curves were fit by a single Boltzmann equation to determine the voltage of half-maximal conductance ($GV_{1/2}$) and apparent valence (Gz). The rate of open-state inactivation was measured by fitting current decay at voltages ≥ -25 mV with a single exponential equation.

We measured the voltage-dependence of fast inactivation as the fraction of current remaining during a test pulse to 0 mV following a 200 ms prepulse to membrane potentials between −130 mV and +10 mV. Normalized current plotted against the voltage during the conditioning pulse was fit by a single Boltzmann equation to determine the voltage of half-maximal fast inactivation ($FIV_{1/2}$) and apparent valence (FIz). To measure the rate of recovery from fast inactivation, currents were recorded during a test pulse to 0 mV following a 200 ms conditioning pulse to 0 mV followed by a variable-length recovery pulse to −90 mV. The current amplitude, plotted as a function of recovery pulse duration, was fit by a bi-exponential equation with the fast component reported as the time constant of fast inactivation.

Persistent sodium current was measured using a 50 ms depolarization to −20 mV from a pre-pulse potential of −130 mV. A minimum of 30 current recordings were averaged and the persistent sodium current was measured as the average current amplitude during the last 5 ms of the depolarization to −20 mV.

Statistical analysis

All statistical analysis was performed in JMP14 (SAS). Differences between mutant and WT channels for any given parameter were tested using two-factor analysis of variance with variant and temperature as the main factors, and the temperature*variant interaction term used to evaluate differences in temperature sensitivity between variants. *Post hoc* testing was done using a Dunnett's correction for multiple testing with the corresponding WT term as the control value. Significance was evaluated at $P < 0.05$. Reported F-values are those from the two-factor ANOVA and reported T-values are those from the Dunnett's *post hoc* test for variant-specific differences at a given temperature. The time constants of fast inactivation recovery were log-transformed before statistical analysis as the log-transformed values are normally distributed.

Computational modelling

To predict neuronal changes that are induced by the gating abnormalities identified in mutant $Na_v1.1$ channels, we implemented the measured deviations in a Hodgkin–Huxley computational model[26] of spiking cortical pyramidal cells.[27] Analogous to prior work, we used published parameterizations of cortical pyramidal cells against which we normalized empirically measured parameter values.[22]

The full model explained in greater detail in the Supplementary Methods is implemented in Python and freely available online (https://github.com/roschkoenig/SodMod). All modelling results presented here can be reproduced from the example code provided in the online repository, or without installing additional software within the Google Colab environment (https://colab.research.google.com/github/roschkoenig/SodMod/blob/master/example_noteboks/Single_Cell_Simulation.ipynb).

Simulation of neuronal firing and bifurcation analysis

Based on our previous work,[22] we implemented normalized values for the experimentally measured parameters summarized in Table 1. Note that prior models of cortical neurons do not contain persistent sodium currents, and the relative strength of the persistent sodium current relative to fast sodium channel currents may be quantitatively different *in vivo* compared to our expression model. Therefore, in a first step, we ran a parameter sweep to identify the appropriate scaling of the persistent sodium current. For this purpose, we systematically varied input current I_{stim} and a multiplicative constant σ_{NaP} that scaled the relative contribution of the persistent sodium channel relative to the overall maximum sodium conductance equally across the different model parameterizations. Full mapping for the parameter sweep is shown in Supplementary Fig. S2. From this parameter sweep, we identified a value for $\sigma_{NaP} = e^{-2.5}$ for which all three neuronal subtypes showed firing at for some values of I_{stim}.

We then implemented one single-compartment neuron for each of the parameterizations given by the empirical measurements (further details given in Supplementary Methods) and the scaling constants identified above, to simulate neuronal responses at different levels of stimulus current input ranging in exponentially spaced intervals from ∼0.002 nA to ∼400 nA. After the simulation reaches a steady-state, minimum and maximum values of the voltage changes and the frequency of neuronal firing events were recorded for bifurcation analysis. Using the last combination of time-varying state values as initial conditions for the next step, we ran this bifurcation analysis forward and backwards to identify possible bistable regimes in the model.

Ethical approval

This study was approved by the hospital ethics committee and informed parental consent to collect clinical data, video recordings and perform genetic and electrophysiology testing was obtained (12.008).

Data availability statement

All data, including numerical simulation results, and code to reproduce the computational analysis are available in

Table 1 Modelling parameters for Hodgkin–Huxley implementation

Parameter (unit)	Value (shared)	Parameter (unit)	WT, 37°C	T783I, 37°C	A1685S, 37°C
C_m (μF/cm^2)	1.0	r_{NaP}	0.019	0.066	0.019
E_K (mV)	−90.0	V_{2m} (mV)	−16.4	−16.1	−11.0
E_{Na} (mV)	55.0	s_m	4.5	4.0	4.2
E_L (mV)	−70.0	V_{2h} (mV)	−50.2	−50.8	−43.5
V_t (mV)	−63.0	s_h	−4.4	−4.0	−4.5
A (cm^2)	0.00029				
g_K (mS/cm^2)	10.0				
g_{Na} (mS/cm^2)	50.0				
g_M (mS/cm^2)	0.07				
g_L (mS/cm^2)	0.10				

Baseline model parameters (shared values on the left) were taken from previously published models of cortical pyramidal cell neurons.[27,28] Empirical recordings were implemented in the model parameters on the right, where the final parameters preserve absolute difference in V_{2m}, and relative differences in s_m, between conditions.
Parameters represent: A = cell surface area; C_m = membrane capacitance; E_K = potassium reversal potential; E_L = leak current reversal potential; E_{Na} = sodium reversal potential; g_K = maximum potassium conductance; g_L = maximum conductance for leak current; g_M = maximum conductance for M-type potassium current; g_{Na} = maximum sodium conductance; s_h = slope at half-maximal fast inactivation; s_m = slope at half-maximal conductance; τ_M = time constant of M-type potassium current; V_{2h} = half-maximal fast inactivation potential; V_{2m} = half-maximal conductance potential; V_t = firing threshold.

a public repository (https://doi.org/10.17605/OSF.IO/YS5RG). Computational analysis can be repeated in-browser without installing additional software in the Google Colaboratory environment (https://bit.ly/SodModNotebook).

Results

Whole-exome sequencing

Two variants were identified in *SCN1A* (ENST00000303395, GenBank: NM_001165963). One variant was previously identified on commercial testing: c.5053C>A; p. A1685S (chr2:165992222, rs760249153) and inherited from the patient's asymptomatic father. A second *de novo* mosaic (18%) missense variant was identified c.2345G>A; p. T782I (chr2:166041301). The mosaic p. T782I variant (15%) was also identified in skin fibroblasts. The p. A1685S variant is classified as a variant of uncertain significance. The p. T782I variant is classified as likely pathogenic as per American College of Medical Genetics criteria[29] (Supplementary Table S1). Long-range PCR confirmed that the *de novo* variant (c.2345G>A) was present in the maternally inherited allele and therefore biallelic. No additional disease-causing or likely disease-causing variants were identified.

Sodium channel dynamics

To investigate the effects of the T782I and A1685S mutants on Nav1.1 gating, we performed whole-cell patch-clamp experiments in CHOK1 cells transfected with WT, T782I, A1685S or both T782I and A1685S (TI-AS) *SCN1A* at 32°C and 37°C. Both the T782I and A1685S mutants produced functional channels at 32°C and 37°C (Fig. 4A1–B4). Peak current at membrane potentials between −100 mV and +40 mV was used to calculate the conductance-voltage (GV) relationship for WT and mutant channels at 32°C and 37°C (Fig. 4C and D, respectively; Table 2). There was a significant mutant-dependent effect on the voltage of half-maximal conductance ($GV_{1/2}$) at 32°C (Fig. 4E; two-factor ANOVA, $F = 3.641$, $P = 0.0163$) due to a significant hyperpolarisation in the $GV_{1/2}$ of the TI-AS channels (Dunnett's *post hoc* test, $T = 3.206$, $P = 0.0019$). There were no significant variant-dependent differences in the ($GV_{1/2}$) for T782I, A1685S or TI-AS channels at 37°C (Fig. 4E; two-factor ANOVA, $F = 1.9368$, $P = 0.1305$). There were no significant temperature-dependent shifts in the half-maximal voltage for any of the channels, consistent with our previous study (Fig. 4E; two-factor ANOVA, $F = 1.4782$, $P = 0.2277$).[22] There was a significant temperature-dependent increase in the apparent valence (Gz) of the GV curve indicating a steeper relationship at 37°C (two-factor ANOVA, $F = 7.2902$, $P = 0.0085$); however, this effect did not differ significantly between channel variants (two-factor ANOVA, $F = 0.4446$, $P = 0.7218$). There were no significant differences in the average current amplitude due to temperature (Fig. 4F; Table 2; two-factor ANOVA, $F = 3.2523$, $P = 0.0751$) or variant (two-factor ANOVA, $F = 1.2291$, $P = 0.3047$). Because the A1685V variant leads to non-functional channels, the lack of effect of A1685S on current amplitude was particularly surprising.[30]

To investigate the effects of T782I and A1685S on fast inactivation, we measured the voltage-dependence of fast inactivation, rate of recovery from fast inactivation at −90 mV, and rate of inactivation onset between −25 mV and + 40 mV. There was a significant variant-dependent shift in the midpoint of the fast inactivation voltage-dependence ($FIV_{1/2}$) at 32°C (Fig. 5A; Table 2; two-factor ANOVA, $F = 4.1412$ $P = 0.0092$) due to a hyperpolarization of the TI-AS midpoint (Dunnett's *post hoc*, $T = 3.336$, $P = 0.0014$). At 37°C there was a non-significant trend towards depolarization in the $FIV_{1/2}$ of A1685S compared to WT (Fig. 5B; Dunnett's *post hoc*,

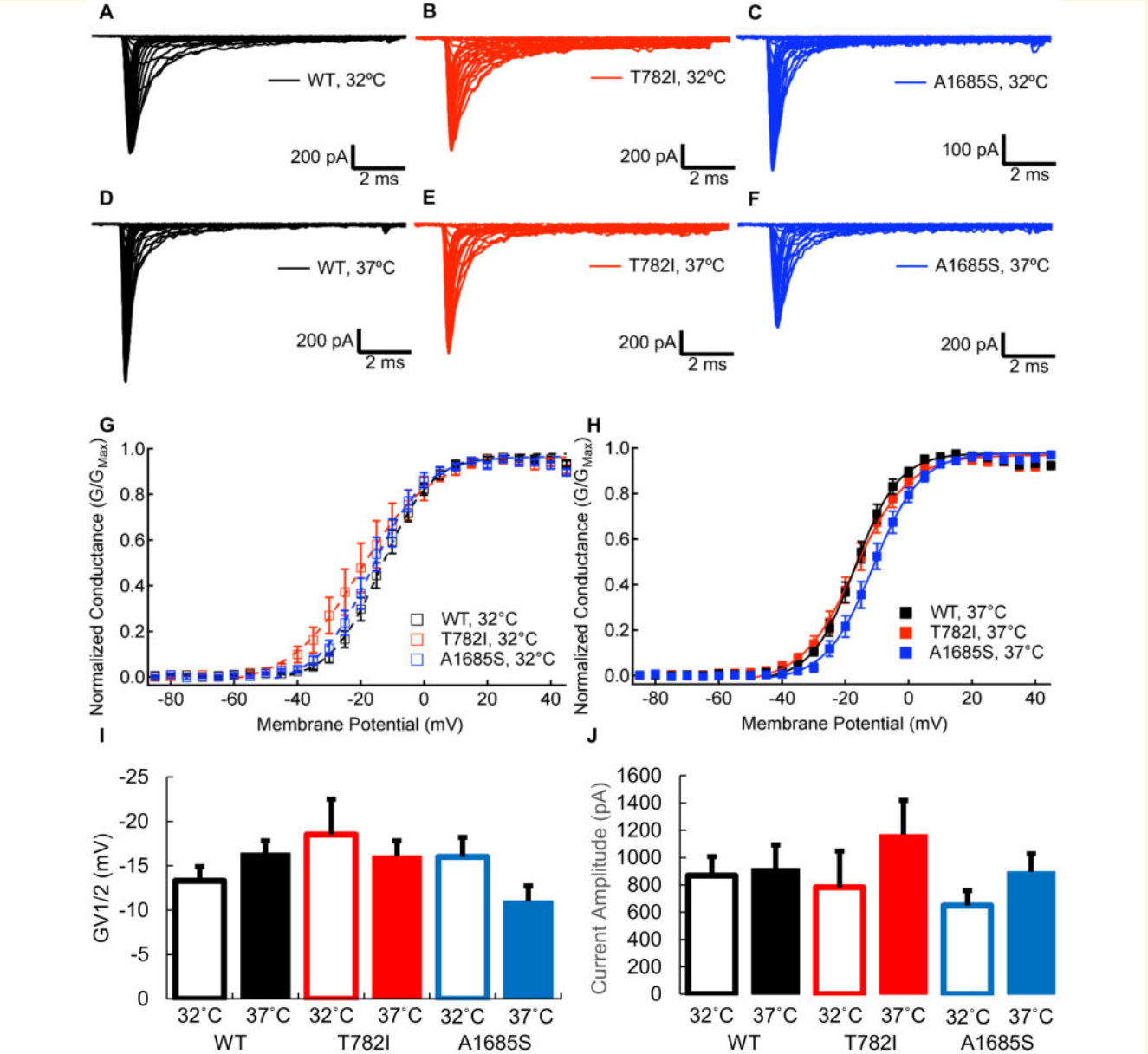

Figure 4 T782I and A1685S mutants in Nav1.1 produce functional channels. (**A,B**) Macroscopic inward currents during depolarizing steps from a holding potential of −130 mV through WT, T782I, A1685S and co-transfected T782I-A1685S Nav1.1 at 32°C and 37°C. (**C**) Conductance-voltage relationships for WT (*black*), T782I (*red*), A1685S (*blue*) and co-transfected T782I-A1685S (purple) Nav1.1 at 32°C. (**D**) Conductance-voltage relationships for WT, T782I, A1685S and co-transfected T782I-A1685S Nav1.1 at 37°C using the same colour scheme as (**C**). (**E**) Average voltage of half-maximal conductance for WT (*black*; $N = 12$ at 32°C; $N = 13$ at 37°C), T782I (*red*; $N = 10$ at 32°C; $N = 13$ at 37°C), A1685S (*blue*; $N = 9$ at 32°C; $N = 9$ at 37°C) and co-transfected T782I-A1685S (purple; $N = 10$ at 32°C; $N = 10$ at 37°C) Nav1.1 at 32°C (open symbols) and 37°C (closed symbols). Individual observations in each condition are shown as smaller symbols. (**F**) Average peak current at 0 mV for WT, T782I, A1685S and co-transfected T782I-A1685S Nav1.1 at 32°C and 37°C using the same colour scheme as (**F**). The number of observations in (**F**) are the same for each condition as in (**F**). Individual observations in each condition are shown as smaller symbols. Each midpoint measurement reflects a mean and each error bar reflects a standard error of the mean. Independent replicates are individual cells recorded in the whole-cell patch clamp configuration. * indicates a statistically significant difference between two midpoints. All statistical analysis was performed with a two-factor ANOVA followed by a Dunnett's *post hoc* of pairwise comparisons to WT. Exact *P*-values and details of statistical tests are found in the main text. Number of individual replicates, means and standard error of the mean for all conditions are found in Table 2 and https://doi.org/10.17605/OSF.IO/YS5RG.

Table 2 Sodium channel dynamics

	WT 37°C	T782I 37°C	A1685S 37°C	TI/AS 37°C
Half-maximal conductance (mV)	−16.4 ± 1.4 (*N* = 13)	−16.1 ± 1.7 (*N* = 13)	−11.0 ± 1.7 (*N* = 9)	−20.2 ± 4.2 (*N* = 10)
Current amplitude (pA)	919 ± 175 (*N* = 14)	1168 ± 251 (*N* = 13)	895 ± 132 (*N* = 9)	1393 ± 308 (*N* = 10)
Half-maximal fast inactivation (mV)	−50.2 ± 1.8 (*N* = 12)	−50.8 ± 1.7 (*N* = 10)	−43.5 ± 2.2 (*N* = 8)	−51.8 ± 3.6 (*N* = 9)
Fast inactivation recovery (ms)	1.3 ± 0.2 (*N* = 11)	1.5 ± 0.2 (*N* = 11)	1.1 ± 0.1 (*N* = 9)	1.3 ± 0.2 (*N* = 7)
Fast inactivation onset (ms)	0.36 ± 0.05 (*N* = 13)	0.41 ± 0.09 (*N* = 12)	0.62 ± 0.13 (*N* = 8) *P* = 0.0216 versus WT	0.23 ± 0.03 (*N* = 9) *P* = 0.0418 versus WT
Persistent current (% of peak)	1.9 ± 0.4 (*N* = 7)	6.6 ± 1.2 (*N* = 7) *P* = 0.0006 versus WT	1.9 ± 0.4 (*N* = 5)	7.1 ± 1.5 (*N* = 6) *P* = 0.0003 versus WT

Mean ± standard error of the mean for key measures of sodium channel dynamics in wildtype (WT), T782I, A1685S and co-transfected T782I-A1685S (TI/AS) channel variants at 37°C. Current amplitude was measured at 0 mV, fast inactivation recovery was measured at −90 mV, fast inactivation onset was measured at 0 mV, and persistent current was measured at −20 mV. *P*-values are derived from Dunnett's *post hoc* tests and listed for measurements that differed significantly from WT. T-values and all other *P*-values can be found within the text. Independent replicates are individual cells recorded in the whole-cell patch clamp. Data can be found at https://doi.org/10.17605/OSF.IO/YS5RG.

$T = 1.9742$, $P = 0.0522$). There was a significant temperature-dependent depolarization of the FIV½ in TI-AS (two-factor ANOVA, $F = 4.5459$, $P = 0.0365$) and a non-significant trend in A1685S Nav1.1 (two-factor ANOVA, $F = 3.7214$, $P = 0.0577$) while WT channels showed no shift, consistent with our previous data.[22] At 32°C and 37°C the FIV½ in T782I Nav1.1 did not significantly differ from WT (Dunnett's *post hoc* test, $T = 0.6300$, $P = 0.5305$; Dunnett's *post hoc* test, $T = 0.1840$, $P = 0.8548$). Consistent with the phenotype of temperature-triggered seizure activity, increasing the temperature to 37°C significantly increased the rate of fast inactivation recovery for all Nav1.1 variants (Figs 5C and 3D; Table 2; two-factor ANOVA, $F = 54.5385$, $P < 0.0001$). There were no significant variant-dependent differences in the fast time constant of fast inactivation recovery at 37°C (two-factor ANOVA, $F = 0.9068$, $P = 0.4427$); however T782I and TI-AS significantly slowed the slow time constant of fast inactivation recovery at 37°C (Dunnett's *post hoc* test, $T = 3.1824$, $P = 0.0022$; Dunnett's *post hoc* test, $T = 2.3196$, $P = 0.0235$). Between -20 mV and +10 mV there were significant variant-dependent shifts in the rate of fast inactivation onset at 37°C (Fig. 5F; Table 2; two-factor ANOVA, $F \geq 3.8536$, $P \leq 0.0130$). This was due to a significant acceleration of the fast inactivation onset in TI-AS between -20 mV and 0 mV (Dunnett's *post hoc* test, $T \geq 2.024$, $P \leq 0.0468$) as well as a significant slowing of the fast inactivation onset rate in A1685S between -10 mV and +10 mV (Dunnett's *post hoc* test, $T \geq 2.174$, $P \leq 0.0330$). T782I did not significantly differ from WT at any of the measured potentials (Dunnett's *post hoc* test, $T \leq 1.275$, $P \geq 0.2066$). At membrane potentials more positive than +10 mV there were no variant-dependent shifts in the rate of fast inactivation onset at either 32°C and 37°C (Fig. 5E and F; two-factor ANOVA, $F \leq 2.7036$, $P \geq 0.0525$).

To measure non-inactivating current, we averaged the current amplitude during the last 5 ms of 50 ms depolarizations to −20 mV (Fig. 6A–E). The fraction of non-inactivating current was determined by normalizing the non-inactivating current to peak current (Fig. 6F; Table 2). T782I induced a large amplitude non-inactivating current that represented greater than 4.5% of the peak current. At 32°C the fraction of non-inactivating current was significantly greater in T782I compared to WT (Fig. 6F; Dunnett's *post hoc* test, $T = 2.370$, $P = 0.0226$). At 37°C the amplitude and fraction of non-inactivating current were significantly greater in T782I Nav1.1 than in WT (Dunnett's *post hoc* test, $T = 3.178$, $P = 0.0029$; Dunnett's *post hoc* test, $T = 3.705$, $P = 0.0006$). There was a significant temperature-dependent increase in the amplitude of the non-inactivating current in T782I at 37°C compared to 32°C (two-factor ANOVA, $F = 6.3863$, $P = 0.0156$). Neither the amplitude nor fraction of non-inactivating current increased in WT as temperature was increased (two-factor ANOVA, $F = 0.0014$, $P = 0.9705$; two-factor ANOVA, $F = 0.0486$, $P = 0.8269$, respectively). Neither the amplitude nor fraction of non-inactivating current in A1685S Nav1.1 differed from WT at either temperature (Dunnett's *post hoc* test, $T \leq 0.1777$, $P \geq 0.8599$). As with T782I alone, the TI-AS co-transfected cells showed significantly larger amplitudes and fractions of non-inactivating current compared to WT at 32°C and 37°C (Dunnett's *post hoc* test, $T \geq 3.014$, $P \leq 0.0045$).

Computational-modelling

We normalized the observed differences in sodium channel gating behaviour and implemented the normalized parameter values in single compartment Hodgkin–Huxley models of neuronal function. This process allowed us to run *in silico* simulations to predict the effects of

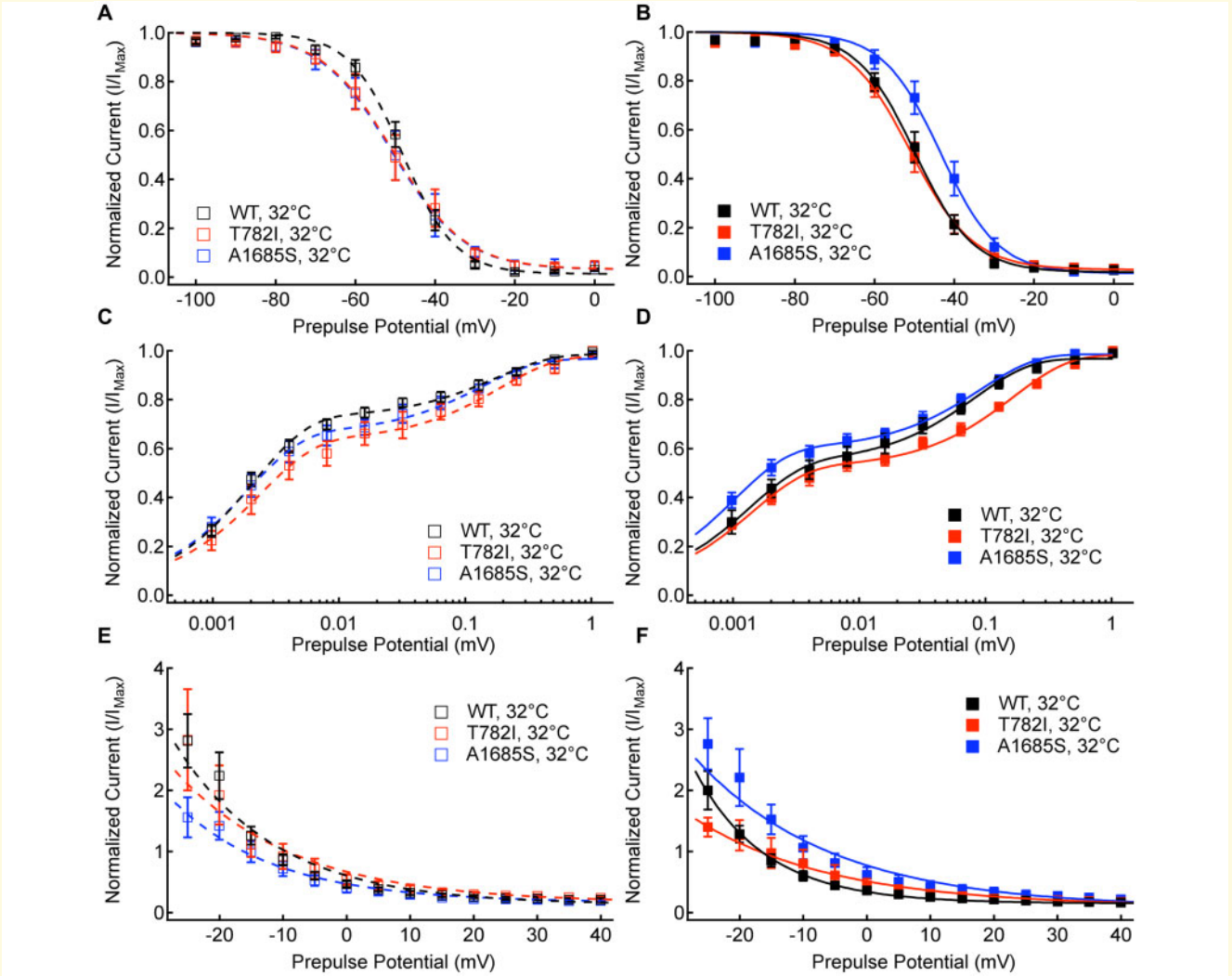

Figure 5 T782I and A1685S mutants in Nav1.1 minimally alter fast inactivation. (**A**) Fast inactivation voltage-dependence for WT (black, $N = 11$), T782I (red, $N = 8$), A1685S (blue, $N = 8$) and co-transfected T782I-A1685S (purple, $N = 10$) Nav1.1 at 32°C. (**B**) Fast inactivation voltage-dependence for WT ($N = 12$), T782I ($N = 12$), A1685S ($N = 9$) and co-transfected T782I-A1685S ($N = 9$) Nav1.1 at 37°C using the same colour scheme as (**A**). (**C**) Time course of fast inactivation recovery at −90 mV for WT ($N = 11$), T782I ($N = 8$), A1685S ($N = 9$) and co-transfected T782I-A1685S ($N = 7$) Nav1.1 at 32°C using the same colour scheme as (**A**). (**D**) Time course of fast inactivation recovery at −90 mV for WT ($N = 11$), T782I ($N = 11$), A1685S ($N = 9$) and co-transfected T782I-A1685S ($N = 7$) Nav1.1 at 37°C using the same colour scheme as (**A**). (**E**) Time constants of fast inactivation onset for WT ($N = 11$), T782I ($N = 8$), A1685S ($N = 7$) and co-transfected T782I-A1685S ($N = 10$) Nav1.1 at 32°C using the same colour scheme as (**A**). (**F**) Time constants of fast inactivation onset for WT ($N = 13$), T782I ($N = 12$), A1685S ($N = 8$) and co-transfected T782I-A1685S ($N = 9$) Nav1.1 at 37°C using the same colour scheme as (**A**). Each mid-point measurement represents a mean and each error bar represents a standard error of the mean. Independent replicates are individual cells recorded in the whole-cell patch clamp configuration. Number of individual replicates, means and standard error of the mean for all conditions are found in Table 2 and https://doi.org/10.17605/OSF.IO/YS5RG.

abnormal sodium channel gating identified in the mutant channels on neuronal firing behaviour.

In the first simulation, we ran the single compartment models with an increasing current ramp as the input current I_{stim} (Fig. 7A). The T782I mutant was clearly hyperexcitable, with sustained high-frequency firing even at the lowest level of current input, an effect visible also in the T782I-A1685S model. All simulated neurons underwent depolarization block once mutation-specific high input current thresholds were exceeded, with the upper threshold being notably increased in the A1685S mutants.

We further explored the dynamic range of the different parameterizations by running repeated simulations with input currents I_{stim} ranging from approximately 0.002 nA to 400 nA (e^{-6} to e^{6}) in exponentially spaced steps in order to visualize the bifurcation behaviour of each of the parameterized models. We can partially visualize the limit cycles for each model during oscillatory dynamics

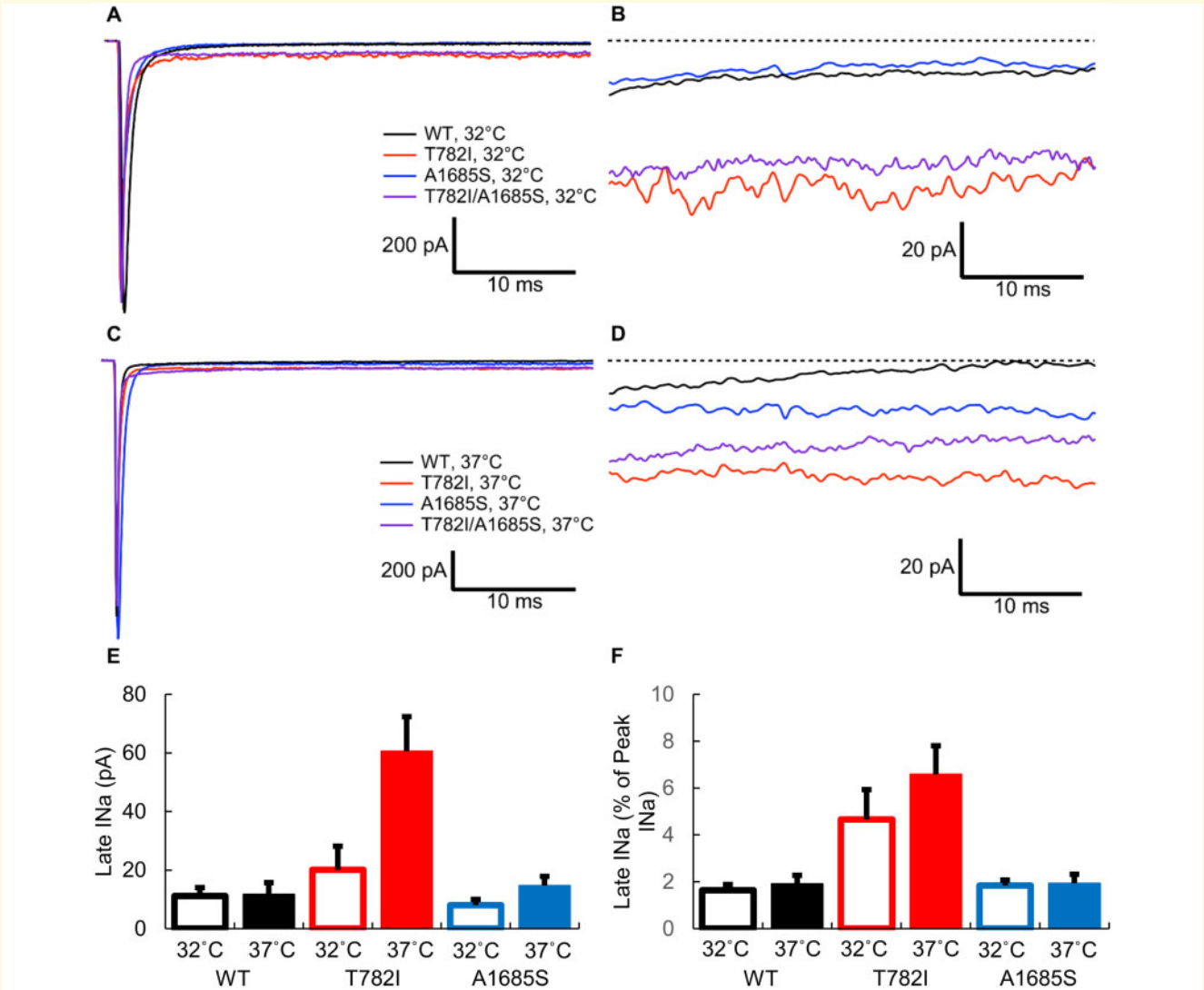

Figure 6 (**A**) Sample currents at −20 mV from WT (black), T782I (red), A1685S (blue) and co-transfected T782I-A1685S (purple) Nav1.1 at 32°C. (**B**) Sample non-inactivating currents at −20 mV in WT, T782I, A1685S and co-transfected T782I-A1685S Nav1.1 at 32°C using the same colour scheme as (**A**). (**C**) Sample currents at −20 mV from WT, T782I, A1685S and co-transfected T782I-A1685S Nav1.1 at 37°C using the same colour scheme as (**A**). (**D**) Sample non-inactivating currents at −20 mV in WT, T782I, A1685S and co-transfected T782I-A1685S Nav1.1 at 37°C using the same colour scheme as (**A**). Note the A1685S cell shown had a larger peak current than the WT cell. **E**) Average amplitude of non-inactivating current at −20 mV for WT ($N = 8$ at 32°C; $N = 7$ at 37°C), T782I ($N = 6$ at 32°C; $N = 7$ at 37°C), A1685S ($N = 4$ at 32°C; $N = 5$ at 37°C) and co-transfected T782I-A1685S ($N = 6$ at 32°C; $N = 6$ at 37°C) Nav1.1 at 32°C (open symbols) and 37°C (closed symbols) using the same colour scheme as (**A**). Individual observations in each condition are shown as smaller symbols. (**F**) Average fraction of non-inactivating current at −20 mV normalized to peak current for WT, T782I, A1685S and co-transfected T782I-A1685S Nav1.1 at 32°C and 37°C using the same colour scheme as (**E**). The number of observations in (**F**) are the same for each condition as in (**E**). Individual observations in each condition are shown as smaller symbols. Each midpoint measurement reflects a mean and each error bar reflects a standard error of the mean. Independent replicates are individual cells recorded in the whole-cell patch clamp configuration. * indicates a statistically significant difference between two midpoints. All statistical analysis was performed with a two-factor ANOVA followed by a Dunnett's *post hoc* of pairwise comparisons to WT. Exact *P*-values and details of statistical tests are found in the main text. Number of individual replicates, means and standard error of the mean for all conditions are found in Table 2 and https://doi.org/10.17605/OSF.IO/YS5RG.

by plotting a subset of temporally changing variables against one another (Fig. 7B). This procedure illustrates that the firing dynamics during low input states were similar for wild type and A1685S channels, whereas T782I channels did not achieve full recovery from inactivation (i.e. *h* values approaching 1) even at the lowest input currents. The T782I-A1685S model most closely resembled the dynamics of T782I.

Bifurcation plots (Fig. 7C) further illustrate the fact that within the tested range there was no stimulating current

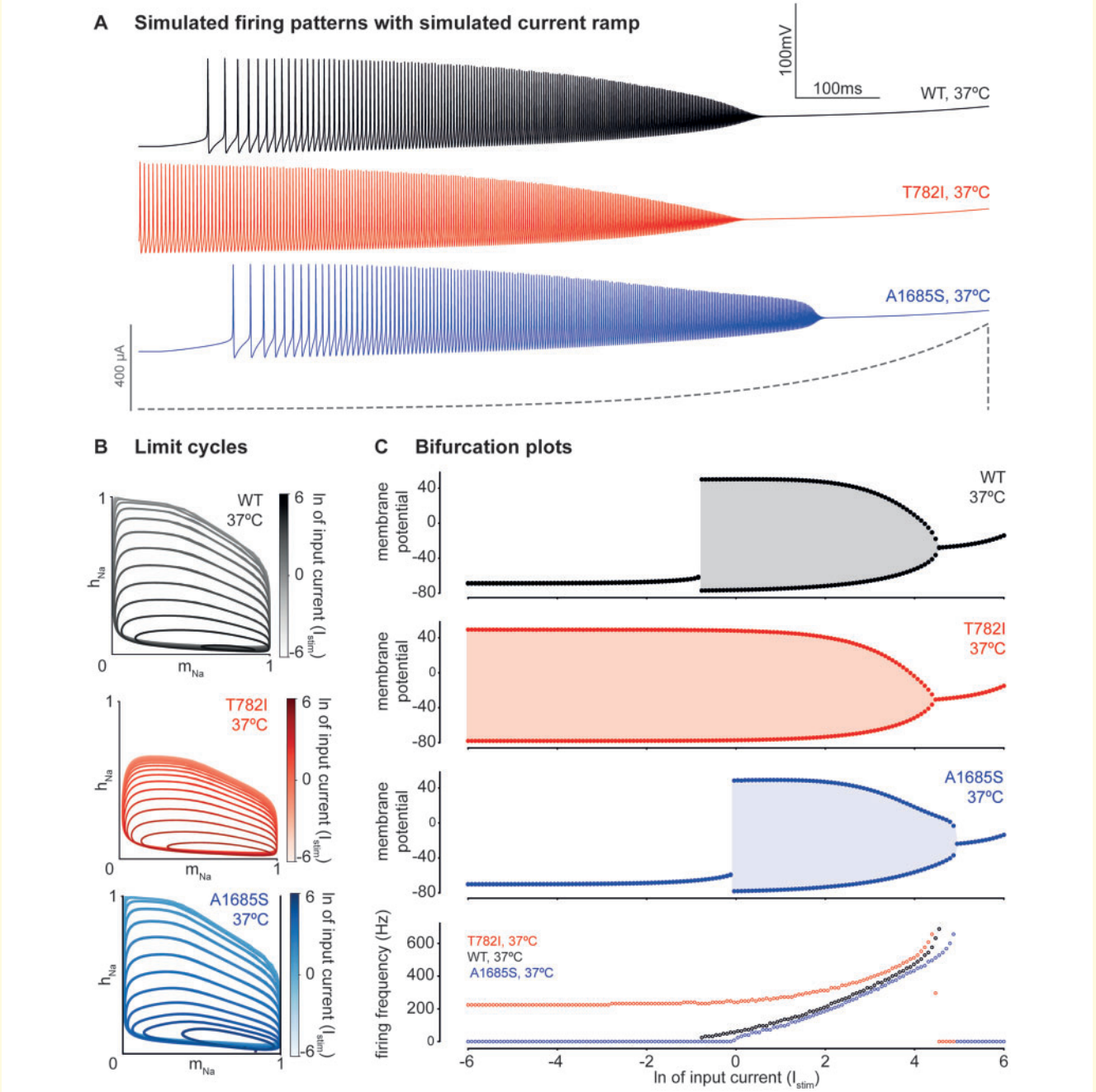

Figure 7 Mutant voltage-gated sodium channels confer differences in neuronal response to stimulation. (**A**) Single compartment neuron simulations for WT and mutant sodium channels with slowly increasing stimulating current I_{stim}. T782I mutant channels confer hyperexcitability at low input current levels, whilst A1685S mutants allow firing even at much higher levels than WT. In the T782I-A1685S model, the effects of T782I predominate. (**B**) Gating variables plotting limit cycles during action potentials at different input current levels. The limit cycles appear similar for wild type and A1685S mutants, whilst T782I and T782I-A1685S do not achieve full inactivation at any input current amplitude. (**C**) Results from repeat simulations at different levels of input currents. Top four plots show maximum and minimum values during the simulated period at steady state, with oscillatory regimes highlighted with shading. The bottom plot shows simulated firing frequency at the different input current levels. Wildtype and A1685S mutants show threshold-like phase transitions at certain I_{stim} values when neuronal firing is initiated. Even at the lowest input currents tested here, both T782I and T782I-A1685S simulated neurons already show fast action potential firing. At very high input currents, all simulated cells cease firing.

I_{stim} for which T782I did not fire. Furthermore, across the entire dynamic range, firing frequency was highest for the T782I-A1685S and the T782I parameteriztions. The plots again indicate that A1685S parameters allowed for the highest input current thresholds before depolarization block occurred (already visible in Fig. 7A).

Discussion

In this article, we identify and characterize biallelic variants in *SCN1A* (paternally inherited p. A1685S variant of uncertain significance, and a *de novo* mosaic p. T782I likely pathogenic variant) associated with a developmental and degenerative epileptic-dyskinetic encephalopathy distinct from the more frequently described DS. In contrast to our current understanding of seizure disorders associated with $Na_v1.1$ predominantly causing channel LOF,[31] we find that both A1685S and T782I elicit GOF properties: a small depolarization in the midpoint of fast-inactivation in A1685S and a large persistent current in T782I. Computational modelling suggests that these changes enable T782I-expressing neurons to fire action potentials at a high-frequency, even in the absence of a stimulatory current, whereas A1685S neurons will continue firing at high current inputs when WT neurons would exhibit depolarization block. This work further expands the spectrum of *SCN1A* variants in childhood seizure disorders, strengthening the emerging evidence[20] that GOF variants, such as T782I, cause a severe DEE, and further highlighting the value of combining *in vitro* and *in silico* experimentation in the explanation and prediction of clinical outcome.

In 80% of cases, *SCN1A* associated epileptic encephalopathies are caused by *de novo* variants in $Na_v1.1$,[32,33] with many variants leading to frameshifted or truncated channels that are presumed to be non-functional.[32,34] The apparent contradiction between increased neural network excitability and LOF in a gene that is generally considered excitatory at the cellular level is typically explained with the disinhibition hypothesis. LOF in $Na_v1.1$ leads to lower firing in inhibitory GABAergic interneurons where $Na_v1.1$ is particularly critical for firing.[8,31,35] Decreased firing in these neurons results in decreased GABA release and greater neural excitability in other brain regions. LOF in $Na_v1.1$ has been studied in animal models, including *Drosophila melanogaster*, zebrafish and mice, with results that are broadly consistent with disinhibition-related epileptogenesis in $Na_v1.1$ haploinsufficiency and LOF.[31,36–39]

Although the disinhibition hypothesis offers a consistent explanation for epileptogenesis in $Na_v1.1$ haploinsufficiency and LOF, it may not be the only pathophysiological mechanism in *SCN1A*-related epilepsies. There is evidence that DS patient-derived neurons may display increased sodium currents and increased firing, even in the absence of a faulty GABAergic system.[40] These cases may represent an *SCN1A*-related epileptic encephalopathy distinct from DS, as seen in our patient. However, given a lack of strong genotype–phenotype correlations in *SCN1A* variants,[18] identifying this putative subgroup in the clinical setting is challenging. Additional characterization of potential biophysical mechanisms associated with epileptogenesis across a diverse group of $Na_v1.1$ mutants is now necessary to help more clearly identify phenotypic subgroups in *SCN1A*-related epilepsies.

Though more comprehensive *in silico* tools now allow for accurate predictions of whether a variant is disease-causing, the ability to discern severity and clinical phenotype is still better predicted by functional characterization through electrophysiology assays.[21,41] Of the greater than 1200 known *SCN1A* variants,[18] only 58 missense variants have been functionally characterized by whole-cell patch-clamp experiments.[21] Approximately, 70% of these cause a LOF. Variants that completely abolish function tend to be associated with classical DS, whereas those which retain some residual current are associated with milder phenotypes like GEFS+.[21] Variants that cause a mixture of LOF and GOF in $Na_v1.l$ biophysics show more varied phenotypes (Supplementary Table S2). Of the 15 previously characterized mixed or GOF variants, 8 were associated with classical DS, 1 with early-onset *SCN1A* DEE, 5 with GEFS+, and one with both DS and GEFS+.[21] This wide variety of changes to $Na_v1.l$ gating in these variants complicate prediction of the resulting changes in cellular excitability, highlighting the importance of modelling and techniques like a dynamic clamp.[20]

Non-inactivating currents occur in approximately 50% of these mixed LOF and GOF variants (Supplementary Table S2). In fact, the original description of channel function in missense variants in DS showed that two variants lead to non-functional channels and two others had mixed properties, primarily GOF with persistent sodium current like that noted here.[23] However, a direct correlation between non-inactivating current amplitude and clinical phenotype in many variants characterized to date is complicated by additional effects on channel function. We show that the T782I variant causes a large amplitude non-inactivating current (>4%) and a severe DEE. This finding is consistent with previous studies of the homologous DEE mutants in *SCN2A* (T773I) and *SCN8A* (T767I), both of which caused an increase in non-inactivating current.[42,43] Ultimately, our data suggest that increases in persistent sodium currents may represent a GOF mechanism associated with severe epilepsy phenotypes even if channel function is otherwise largely preserved.

When incorporated into a pyramidal neuron model, the large non-inactivating current in T782I causes action potential firing even in the presence of arbitrarily low input currents. Furthermore, the T782I simulations show neuronal firing characteristics—in terms of limit cycle shape—that are observed only at much higher input currents in either WT or A1685S simulations. The simulated T782I neurons fire at high frequency and never achieve full recovery from inactivation, even at the lowest input regime. High-frequency firing is seen in the other simulations only at input currents that are orders of magnitude higher. The T782I simulations also show higher firing

frequencies across their entire dynamic range compared to the other simulations.

The increased excitability of neurons within our *in silico* models is consistent with *in vivo* results that show persistent sodium current stabilizes repetitive firing in neurons by lowering the threshold for spike generation.[44] When non-inactivating sodium currents are inhibited by blockers, the ability of neurons to fire repetitive action potentials is inhibited, while the generation of individual spikes in response to a transient stimulus is maintained.[45] *In vivo*, non-inactivating sodium currents play a physiological role in determining repetitive firing, amplifying post-synaptic potentials and generating rhythmicity.[44–47] Indeed, the brain sodium channels ($Na_v1.1$, $Na_v1.2$ and $Na_v1.6$) have all been shown to produce relatively large fractions of non-inactivating current.[48,49] In contrast to this physiological role, our data support the notion that T782I confers pathological increases in non-inactivating current, which may be capable of driving the severe DEE observed in our patient.

While less severe than the T782I variant and likely not causative, the A1685S simulations clearly show a distinct picture. The A1685S neuronal dynamics, including the oscillatory onset bifurcation and the firing frequency, are similar to the WT in low input regimes. However, at high inputs, A1685S simulated neurons continue to fire, even when the other simulations have undergone complete depolarization block. Once again, this behaviour suggests a milder GOF picture associated with this missense variant, although this is tolerated in the unaffected parent from which the variant was inherited with the same variant and also reported in population databases[50]

The neuronal firing changes predicted here suggest profound hyperexcitability of affected neurons. This hyperexcitability may have epileptogenic effects either directly through the involvement of excitatory neurons, or by inducing paradoxical GABAergic excitation during excessive activation states as previously described during refractory status epilepticus.[51,52] Importantly, the hyperexcitability identified here *in silico* also would render any similarly affected neurons unresponsive to external stimulation, impairing any normal processing and perhaps predisposing to excitotoxicity—all consistent with the devastating clinical phenotype observed in our patient.

Persistent sodium currents have also been associated with neurodegeneration in amyotrophic lateral sclerosis, anoxia and injury-induced neurodegeneration.[53–55] In these models, persistent currents are predicted to cause intracellular calcium through the activation of the sodium–calcium exchanger. This in turn activates calcium-dependent enzymes yielding permanent cell injury. Treatment with sodium channel blockers has proved effective at limiting neurodegeneration.[56–58] These data are consistent with the progressive clinical course and brain atrophy noted in the MRI at age 4 years (Supplementary Fig. S1); suggesting an additional mechanism of neurodegeneration in GOF induced DEE.

The frequency of mosaic pathogenic variants in *SCN1A* in affected probands is 1.3%.[59] The identification of mosaicism, like in this case, has improved with next-generation sequencing and targeted deep resequencing using single-molecule molecular inversion probes.[16] There are a number of papers reporting individuals with low-level of mosaicism in *SCN1A* and severe disease, including DS.[15,16,59] A summary of mosaic variants in *SCN1A* and the associated phenotypes are listed in Supplementary Table S3. Mosaic variants in DS are reported between 15.2% and 39% in blood.[15,16,59] Mosaicism is reported in other DEE genes with a severe phenotypes including: *SCN2A* and Ohtahara syndrome (blood—18%), *GRIN1* and DEE (blood—19.7%, saliva—16.8%, hair roots—19.7% and nail—13.4%) and *ATP1A3* and DEE (blood—26.2%).[60–62] In fact, the patient carrying the mosaic *SCN2A* variant (18% mosaicism) reported by (60) is predicted to be a GOF,[24] and presented within the first days of life with Ohtahara syndrome, with the early onset being suggestive of GOF pathogenic variants.[33]

Marked differences in phenotypic severity associated with mosaicism are explained in part by variation in mosaicism levels in disease-relevant tissues. The affected individual in our report, had fibroblast and blood tested. Post-mortem was not performed, therefore brain tissue was not available, to test the level of mosaicism in the affected tissue. However, we assume a similarly affected percentage in brain tissues, the size of the mutant populations, depending on the age and rate of further cell division at the time of the missense variant.

Whilst there is no universally agreed cut-off percentage—particularly for peripheral tissues—at which mosaic variants are considered pathogenic, previous reports in DEEs have demonstrated an epileptic phenotype in patients with similar and lower percentages than reported here. Yet we would expect the severe hyperexcitability caused by the GOF effect of the mutation to produce more severe phenotypes even at low mosaicism levels compared to the previously reported LOF variants (Supplementary Table S3). Specifically, our modelling shows that even in mixed NaV1.1 expression, neurons carrying the T782I variant show severe hyperexcitability, rendering a subset of cortical neurons extremely hyperexcitable. Detailed calcium imaging studies of seizure onset in rodent models of genetic generalized epilepsies have already demonstrated that only a small subset (approximately 20%) of neurons activates even at the onset of a generalized seizure.[63] This suggests that constitutive hyperexcitability in a similarly sized subset of neurons would also cause whole-brain disruptions of neuronal function consistent with the severe phenotype observed in the patient reported here.

The later age of onset than typical DS may be correlated with the time course by which the foetal $Na_v1.3$ isoform is replaced with the $Na_v1.1$ isoform. Maximal

$Na_v1.1$ expression occurs between 10 months and 2 years.[7,64] As the T782I variant is mosaic, it may require full replacement of the $Na_v1.3$ isoform with the affected $Na_v1.1$ isoform before the clinical phenotype is observed.

Our patient represents a case of an emerging epileptic encephalopathy associated with mutations in *SCN1A* that is distinct from classical DS. Her initial clinical presentation of normal development in the first year of life, followed by hemi-clonic and clonic prolonged seizures starting aged 13 months, was in keeping with a clinical diagnosis of DS and the reason for commercial single gene testing of *SCN1A*. However, the subsequent clinical course with the emergence of hyperkinetic movement disorder, progressive loss of skills and evolution of EEG were not typical of DS.[12,65] Our patient and those reported with an early-onset *SCN1A* DEE due to GOF variants, have overlapping features of a more severe refractory epilepsy than typical DS, profound global regression early in the course of the disease, a hyperkinetic movement disorder and severe ID (Supplementary Table S4). In light of the clinical phenotype of the case described here, the biophysical characterization and the computational modelling, our results support that GOF *SCN1A* variants, such as T782I, should be recognized as a distinct phenotype to DS, a developmental and degenerative epileptic-dyskinetic encephalopathy. Hyperkinetic movement disorder and a progressive course are distinct and atypical for DS.

SCN1A-related disorders should no longer be viewed as solely a neurodevelopmental disorder or as DEE. The persistent sodium current as characterized in T782I, also initiates neurodegeneration and the progressive clinical presentation with marked regression in skills and hyperkinetic movement disorder in our proband, distinct from DS. Thus, our case highlights the importance of rigorous biophysical evaluation and computational modelling with the clinical phenotype, to understand the phenotypic pleiotropy of pathogenic variants in *SCN1A* and enables accurate counselling of families and potential disease-modifying treatment in the future for children with GOF variants in *SCN1A*.

Supplementary material

Supplementary material is available at *Brain Communications* online.

Acknowledgements

The authors would like to acknowledge the parents for participation in the study and publication of patient data. We would like to acknowledge Drs Saskia Biskup (Cegat GmBh) Kathrin Rothfelder (Cegat GmBh) and Heather Church (Willink Biochemical Genetics Unit).

Funding

K.G. received funding from Temple Street Foundation. C.P., L.J. and P.R. received funding from the British Columbia Rare Disease Foundation, the Dravet Foundation of Canada and the Natural Sciences and Engineering Research Council of Canada. R.R. received funding from the Wellcome Trust (209164/Z/17/Z). D.S.B. received funding from the John D. and Catherine T. MacArthur Foundation.

Competing interests

The authors declare no competing interests.

References

1. Covanis A. Epileptic encephalopathies (including severe epilepsy syndromes). *Epilepsia*. 2012;53 (Suppl 4):114–126.
2. McTague A, Howell KB, Cross JH, Kurian MA, Scheffer IE. The genetic landscape of the epileptic encephalopathies of infancy and childhood. *Lancet Neurol*. 2016;15(3):304–316.
3. Scheffer IE, Berkovic S, Capovilla G, et al. ILAE classification of the epilepsies: Position paper of the ILAE Commission for Classification and Terminology. *Epilepsia*. 2017;58(4):512–521.
4. Absoud M, Parr JR, Halliday D, Pretorius P, Zaiwalla Z, Jayawant S. A novel ARX phenotype: Rapid neurodegeneration with Ohtahara syndrome and a dyskinetic movement disorder. *Dev Med Child Neurol*. 2010;52(3):305–307.
5. Carvill GL, Helbig KL, Myers CT, et al. Damaging de novo missense variants in EEF1A2 lead to a developmental and degenerative epileptic-dyskinetic encephalopathy. *Hum Mutat*. 2020;41(7):1263–1279.
6. Gorman KM, Meyer E, Grozeva D, et al. Bi-allelic loss-of-function CACNA1B mutations in progressive epilepsy-dyskinesia. *Am J Hum Genet*. 2019;104(5):948–956.
7. Cheah CS, Yu FH, Westenbroek RE, et al. Specific deletion of NaV1.1 sodium channels in inhibitory interneurons causes seizures and premature death in a mouse model of Dravet syndrome. *Proc Natl Acad Sci USA*. 2012;109(36):14646–14651.
8. Tai C, Abe Y, Westenbroek RE, Scheuer T, Catterall WA. Impaired excitability of somatostatin- and parvalbumin-expressing cortical interneurons in a mouse model of Dravet syndrome. *Proc Natl Acad Sci USA*. 2014;111(30):E3139–3148.
9. Brunklaus A, Du J, Steckler F, et al. Biological concepts in human sodium channel epilepsies and their relevance in clinical practice. *Epilepsia*. 2020;61(3):387–399.
10. Scheffer IE, Nabbout R. SCN1A-related phenotypes: Epilepsy and beyond. *Epilepsia*. 2019;60 (Suppl 3):S17–24.
11. Carranza Rojo D, Hamiwka L, McMahon JM, Dibbens LM, et al. De novo SCN1A mutations in migrating partial seizures of infancy. *Neurology*. 2011;77(4):380–383.
12. Dravet C. The core Dravet syndrome phenotype. *Epilepsia*. 2011;52:3–9.
13. Escayg A, MacDonald BT, Meisler MH, et al. Mutations of SCN1A, encoding a neuronal sodium channel, in two families with GEFS+2. *Nat Genet*. 2000;24(4):343–345.
14. Sadleir LG, Mountier EI, Gill D, et al.; DDD Study Not all SCN1A epileptic encephalopathies are Dravet syndrome: Early profound Thr226Met phenotype. *Neurology*. 2017;89(10):1035–1042.
15. de Lange IM, Koudijs MJ, van 't Slot R, et al. Mosaicism of de novo pathogenic SCN1A variants in epilepsy is a frequent

phenomenon that correlates with variable phenotypes. *Epilepsia*. 2018;59(3):690–703.
16. Muir AM, King C, Schneider AL, et al. Double somatic mosaicism in a child with Dravet syndrome. *Neurol Genet*. 2019;5(3):e333.
17. Myers CT, Hollingsworth G, Muir AM, et al. Parental mosaicism in 'De Novo' epileptic encephalopathies. *N Engl J Med*. 2018; 378(17):1646–1648.
18. Meng H, Xu H-Q, Yu L, et al. The SCN1A mutation database: Updating information and analysis of the relationships among genotype, functional alteration, and phenotype. *Hum Mutat*. 2015;36(6):573–580.
19. Angus M, Peters CH, Poburko D, Brimble E, Spelbrink EM, Ruben PC. Case studies in neuroscience: A novel amino acid duplication in the NH2-terminus of the brain sodium channel NaV1.1 underlying Dravet syndrome. *J Neurophysiol*. 2019;122(5): 1975–1980.
20. Berecki G, Bryson A, Terhag J, et al. SCN1A gain of function in early infantile encephalopathy. *Ann Neurol*. 2019;85(4):514–525.
21. Brunklaus A, Schorge S, Smith AD, et al. SCN1A variants from bench to bedside-improved clinical prediction from functional characterization. *Hum Mutat*. 2020;41(2):363–374.
22. Peters C, Rosch RE, Hughes E, Ruben PC. Temperature-dependent changes in neuronal dynamics in a patient with an *SCN1A* mutation and hyperthermia induced seizures. *Sci Rep*. 2016;6: srep31879.
23. Rhodes TH, Lossin C, Vanoye CG, Wang DW, George AL. Noninactivating voltage-gated sodium channels in severe myoclonic epilepsy of infancy. *Proc Natl Acad Sci USA*. 2004;101(30): 11147–11152.
24. Heyne HO, Baez-Nieto D, Iqbal S, et al. Predicting functional effects of missense variants in voltage-gated sodium and calcium channels. *Sci Transl Med*. 2020;12:eaay6848.
25. Allen NM, Conroy J, Shahwan A, et al. Unexplained early onset epileptic encephalopathy: Exome screening and phenotype expansion. *Epilepsia*. 2016;57(1):e12–e17.
26. Hodgkin AL, Huxley AF. A quantitative description of membrane current and its application to conduction and excitation in nerve. *J Physiol*. 1952;117(4):500–544.
27. Destexhe A, Contreras D, Sejnowski TJ, Steriade M. A model of spindle rhythmicity in the isolated thalamic reticular nucleus. *J Neurophysiol*. 1994;72(2):803–818.
28. Traub RD, Wong RK, Miles R, Michelson H. A model of a CA3 hippocampal pyramidal neuron incorporating voltage-clamp data on intrinsic conductances. *J Neurophysiol*. 1991;66(2):635–650.
29. Richards S, Aziz N, Bale S, et al.; ACMG Laboratory Quality Assurance Committee. Standards and guidelines for the interpretation of sequence variants: A joint consensus recommendation of the American College of Medical Genetics and Genomics and the Association for Molecular Pathology. *Genet Med*. 2015;17(5): 405–424.
30. Lossin C, Rhodes TH, Desai RR, et al. Epilepsy-associated dysfunction in the voltage-gated neuronal sodium channel SCN1A. *J Neurosci*. 2003;23(36):11289–11295.
31. Oakley JC, Kalume F, Catterall WA. Insights into pathophysiology and therapy from a mouse model of Dravet syndrome. *Epilepsia*. 2011;52 (Suppl 2):59–61.
32. Claes L, Del-Favero J, Ceulemans B, Lagae L, Van Broeckhoven C, De Jonghe P. De novo mutations in the sodium-channel gene SCN1A cause severe myoclonic epilepsy of infancy. *Am J Hum Genet*. 2001;68(6):1327–1332.
33. Wolff M, Johannesen KM, Hedrich UBS, et al. Genetic and phenotypic heterogeneity suggest therapeutic implications in SCN2A-related disorders. *Brain J Neurol*. 2017;140(5):1316–1336.
34. Zuberi SM, Brunklaus A, Birch R, Reavey E, Duncan J, Forbes GH. Genotype-phenotype associations in SCN1A-related epilepsies. *Neurology*. 2011;76(7):594–600.
35. Bender AC, Morse RP, Scott RC, Holmes GL, Lenck-Santini P-P. SCN1A mutations in Dravet syndrome: Impact of interneuron dysfunction on neural networks and cognitive outcome. *Epilepsy Behav*. 2012;23(3):177–186.
36. Baraban SC, Dinday MT, Hortopan GA. Drug screening in Scn1a zebrafish mutant identifies clemizole as a potential Dravet syndrome treatment. *Nat Commun*. 2013;4:2410.
37. Rosch R, Burrows DRW, Jones LB, Peters CH, Ruben P, Samarut É. Functional genomics of epilepsy and associated neurodevelopmental disorders using simple animal models: From genes, molecules to brain networks. *Front Cell Neurosci*. 2019;13:556.
38. Schutte RJ, Schutte SS, Algara J, et al. Knock-in model of Dravet syndrome reveals a constitutive and conditional reduction in sodium current. *J Neurophysiol*. 2014;112(4):903–912.
39. Yu FH, Mantegazza M, Westenbroek RE, et al. Reduced sodium current in GABAergic interneurons in a mouse model of severe myoclonic epilepsy in infancy. *Nat Neurosci*. 2006;9(9): 1142–1149.
40. Liu Y, Lopez-Santiago LF, Yuan Y, et al. Dravet syndrome patient-derived neurons suggest a novel epilepsy mechanism. *Ann Neurol*. 2013;74(1):128–139.
41. Nissenkorn A, Almog Y, Adler I, et al. In vivo, in vitro and in silico correlations of four de novo SCN1A missense mutations. *PLoS One*. 2019;14(2):e0211901.
42. Estacion M, O'Brien JE, Conravey A, et al. A novel de novo mutation of SCN8A (Nav1.6) with enhanced channel activation in a child with epileptic encephalopathy. *Neurobiol Dis*. 2014;69: 117–123.
43. Lauxmann S, Verbeek NE, Liu Y, et al. Relationship of electrophysiological dysfunction and clinical severity in SCN2A-related epilepsies. *Hum Mutat*. 2018;39(12):1942–1956.
44. Deng P-Y, Klyachko VA. Increased persistent sodium current causes neuronal hyperexcitability in the entorhinal cortex of Fmr1 knockout mice. *Cell Rep*. 2016;16(12):3157–3166.
45. Kuo JJ, Lee RH, Zhang L, Heckman CJ. Essential role of the persistent sodium current in spike initiation during slowly rising inputs in mouse spinal neurones. *J Physiol*. 2006;574(Pt 3): 819–834.
46. Schwindt PC, Crill WE. Amplification of synaptic current by persistent sodium conductance in apical dendrite of neocortical neurons. *J Neurophysiol*. 1995;74(5):2220–2224.
47. Taddese A, Bean BP. Subthreshold sodium current from rapidly inactivating sodium channels drives spontaneous firing of tuberomammillary neurons. *Neuron*. 2002;33(4):587–600.
48. Chatelier A, Zhao J, Bois P, Chahine M. Biophysical characterisation of the persistent sodium current of the Nav1.6 neuronal sodium channel: A single-channel analysis. *Pflugers Arch*. 2010; 460(1):77–86.
49. Mantegazza M, Yu FH, Powell AJ, Clare JJ, Catterall WA, Scheuer T. Molecular determinants for modulation of persistent sodium current by G-protein betagamma subunits. *J Neurosci*. 2005;25(13):3341–3349.
50. Karczewski KJ, Francioli LC, Tiao G, et al.; Genome Aggregation Database Consortium. The mutational constraint spectrum quantified from variation in 141,456 humans. *Nature*. 2020;581(7809): 434–443.
51. Burman RJ, Selfe JS, Lee JH, van den Berg M, et al. Excitatory GABAergic signalling is associated with benzodiazepine resistance in status epilepticus. *Brain J Neurol*. 2019;142(11):3482–3501.
52. Khazipov R. GABAergic synchronization in epilepsy. *Cold Spring Harb Perspect Med*. 2016;6(2):a022764.
53. Eijkelkamp N, Linley JE, Baker MD, et al. Neurological perspectives on voltage-gated sodium channels. *Brain*. 2012;135(Pt 9): 2585–2612.
54. LoRusso E, Hickman JJ, Guo X. Ion channel dysfunction and altered motoneuron excitability in ALS. *Neurol Disord Epilepsy J*. 2019;3:124.
55. Stys PK. White matter injury mechanisms. *Curr Mol Med*. 2004; 4(2):113–130.

56. Hewitt KE, Stys PK, Lesiuk HJ. The use-dependent sodium channel blocker mexiletine is neuroprotective against global ischemic injury. *Brain Res*. 2001;898(2):281–287.
57. Kapoor R, Davies M, Blaker PA, Hall SM, Smith KJ. Blockers of sodium and calcium entry protect axons from nitric oxide-mediated degeneration. *Ann Neurol*. 2003;53(2):174–180.
58. Waxman SG, Black JA, Ransom BR, Stys PK. Anoxic injury of rat optic nerve: Ultrastructural evidence for coupling between Na+ influx and Ca(2+)-mediated injury in myelinated CNS axons. *Brain Res*. 1994;644(2):197–204.
59. Stosser MB, Lindy AS, Butler E, et al. High frequency of mosaic pathogenic variants in genes causing epilepsy-related neurodevelopmental disorders. *Genet Med*. 2018;20(4):403–410.
60. Nakamura K, Kato M, Osaka H, et al. Clinical spectrum of SCN2A mutations expanding to Ohtahara syndrome. *Neurology*. 2013;81(11):992–998.
61. Ohba C, Shiina M, Tohyama J, et al. *GRIN1* mutations cause encephalopathy with infantile-onset epilepsy, and hyperkinetic and stereotyped movement disorders. *Epilepsia*. 2015;56(6):841–848.
62. Vetro A, Nielsen HN, Holm R, et al.; ATP1A2/A3-orators. ATP1A2- and ATP1A3-associated early profound epileptic encephalopathy and polymicrogyria. *Brain*. 2021;144(5):1435–1450.
63. Meyer J, Maheshwari A, Noebels J, Smirnakis S. Asynchronous suppression of visual cortex during absence seizures in stargazer mice. *Nat Commun*. 2018;9(1):1938.
64. Smith RS, Kenny CJ, Ganesh V, et al. Sodium channel SCN3A (NaV1.3) regulation of human cerebral cortical folding and oral motor development. *Neuron*. 2018;99(5):905–913.e7.
65. Wirrell EC, Laux L, Donner E, et al. Optimizing the diagnosis and management of Dravet syndrome: Recommendations from a North American consensus panel. *Pediatr Neurol*. 2017;68:18–34.e3.